Research Article Vol. 15, No. 12 / 1 Dec 2024 / Biomedical Optics Express 6877
Biomedical Optics EXPRESS

Quantitative investigations on light emission profiles for interstitial laser treatment

Minh Duc Ta,[1] Yeongeun Kim,[1] Hwarang Shin,[1] Van Gia Truong,[2] and Hyun Wook Kang[1,2,3,4,*]

[1]*Industry 4.0 Convergence Bionics Engineering and Marine-integrated Biomedical Technology Center, Pukyong National University, Busan, Republic of Korea*
[2]*TeCure, Inc., Busan, Republic of Korea*
[3]*Division of Smart Healthcare, College of Information Technology and Convergence, Pukyong National University, Busan, Republic of Korea*
[4]*Marine-integrated Biomedical Technology Center, The National Key Research Institutes in Universities, Pukyong National University, Busan, Republic of Korea*
[*]*wkang@pukyong.ac.kr*

Abstract: Interstitial laser treatment (ILT) using a diffusing applicator (DA) has been employed to treat tumors. However, the treatment efficacy and safety of the emission profiles from DAs have been poorly explored. This study investigated the effect of the emission profiles from DAs on prostate tumor treatment. Dual-peak and proximal-/distal-end peak profiles using 980 nm laser at 5 W for 60 s were tested to compare the extent of thermal coagulation in soft tissue numerically and experimentally. The numerical simulation predicted the temperature development in the tissue. Ex vivo porcine liver and in vivo rat models were used to compare the performance of the profiles. The dual-peak profile yielded a coagulation extent that was almost equivalent to that of the flat-top profile (in simulation) and 1.3 times larger than those of the other profiles in both ex vivo and in vivo. The dual-peak profile predictably entailed uniform coagulation within the irradiated region. Further in vivo studies using different tumor sizes will be evaluated to warrant the efficacy and safety of the dual-peak profile for the ILT of prostate tumors.

1. Introduction

As reported by Global Cancer Observatory (GLOBOCAN), prostate cancer (PC) is the second most common cancer and the second major cause of cancer death worldwide [1–3]. The PC is often diagnosed in 112 countries, with the highest cases in high-income areas, such as North America, Europe, New Zealand, and Australia, and the lowest cases in South Asia [4–6]. The PC forms in men [7]. The age-standardized incidence and mortality rate of PC are 30.7 per 100,000 males and 0.54-41.7 per 100,000 males in 2020, respectively [4]. The highest mortality rate of PC is primarily observed in low-income areas, for example, Africa [8]. In 2022, the estimated number of new PC diagnoses is approximately 1.41 million for men worldwide and 268,490 for American males [7,9–11]. The estimated number of deaths from PC is 34,500 cases, accounting for 11% of all deaths [11]. The predicted new diagnoses will reach 1,700,000 cases, and the death number will be 499,000 in 2030 in the world [3,9]. Moreover, the PC incidence of younger people (age < 50 years) has increased by five times over the past decade [12] due to the gradually rising prevalence of PC risks, for example, alcohol usage, smoking, obesity, reduced physical exercises, and metabolic syndrome [8,13]. The rising trend in the PC incidence leads to increasingly diverse patient circumstances, including various PC stages and a greater demand for personalized treatment strategies. The complexity of the patient circumstances requires advancements in medical devices to ensure the personalized treatment solutions. Thus, the development of effective treatments for PC is necessary to maximize clinical outcomes and to minimize side-effects.

#540470 https://doi.org/10.1364/BOE.540470
Journal © 2024 Received 27 Aug 2024; revised 19 Oct 2024; accepted 5 Nov 2024; published 20 Nov 2024

Biomedical Optics EXPRESS

Thermal treatment (TT) is a well-known technique used for minimally invasive treatment of various cancer types [14]. A number of the TT techniques have been investigated, such as radiofrequency ablation (RFA), microwave ablation (MWA), high intensity-focused ultrasound (HIFU), photodynamic therapy (PDT), and cryotherapy (CT) [14–19]. These techniques differ in terms of physical phenomena in heat generation and the promotion of coagulative necrosis at the targeted tissue. RFA generates coagulative necrosis resulting from ionic agitation and frictional heats by transmitting the RF wave and alternating the current in an insulated electrode tip [20]. Due to the increasing size of the targeted tissue and inhomogeneous tissue properties (e.g., electrical conductivity, dielectric permittivity, and heat-sink effect), RFA suffers from the limitations, such as impedance variations and excessive local heat [21]. MWA delivers the frequency of 900-2,500 MHz to induce heat via oscillation of water molecules in tissue [21]. Although MWA creates more uniform thermal coagulation than RFA, MWA still requires a bulky system with big cables and back-heating effects [21,22]. HIFU is a non-invasive modality and utilizes non-ionizing radiation (i.e., converting mechanical energy into heat) to cause tissue destruction. The efficacy of HIFU is limited by long treating time, penetration depth, and organ movement [17,23]. PDT is a light-induced therapy that combines light excitation and photosensitizer (PS) to destroy the targeted tissue. The drawbacks of PDT include the limited selectivity of the PDT agents, the short penetration depth of light, and tissue oxygenation-dependent efficacy [24–26]. Lastly, CT is a focal therapy inducing tissue injury by immediately freezing tissue with cold gas (liquid nitrogen, liquid nitrous oxide, and compressed argon gas) for ice formation and cellular necrosis at least -40 °C [27,28]. However, the downside of CT includes cryoshock, unfavorable organ fracture, and bleeding complications due to the non-coagulation of injured vessels. Therefore, the existing limitations of these techniques need to be overcome to enhance clinical outcomes and to curtail the associated complications.

Recently, interstitial laser treatment (ILT) has gradually become a promising thermal therapy for PC [16,17,29]. ILT utilizes an optical diffusing applicator (DA) to deliver light into a tumor with high precision. High temperature from light-tissue interaction forms a volume of irreversible thermal necrosis. Various imaging-guided techniques were combined with ILT to enhance the efficacy and safety of ILT. As a result, ILT can be a feasible alternative to treat low or moderate-risk PC [16]. However, as a single DA yields only a few centimeters of treatment range and is affected by heat-sink effect [16,20,22,23], ILT presents risks in larger tumors and crucial organs surrounding the tumor. Additionally, a non-uniform light emission profile is a challenge for warranting the irradiation accuracy of DA application. The non-uniform profile along the DA could produce irregular and unpredictable coagulation in tissue, leading to unfavorable thermal injury to the adjacent healthy tissue [30]. Nevertheless, there is a lack of studies (or few studies) that have explored the impact of the emission profile from DA on predicting temperature variations and the formation of the thermal coagulation after ILT [31]. Thus, a uniform light emission profile (also known flat-top profile), as well as ability to fabricate different light profiles along the DA length is often desired to select and minimize these risks on varying in size and shape of the tumor [31–33]. The purpose of the current study was to investigate the effect of three different emission profiles (i.e., dual-peak, proximal-end peak, and distal-end peak) from DAs on ILT of prostate cancer both numerically and experimentally. To compare the performance of the emission profiles, 980 nm wavelength laser light was employed. The extent of the thermal coagulation in tumor tissue was compared through simulations, ex vivo, and in vivo experiments.

2. Materials and methods

2.1. Numerical simulations

Numerical simulations were performed to predict spatio-temporal developments of temperature and thermal damage in tissue during laser irradiation by using COMSOL Multiphysics software (v5.6, COMSOL, Inc., Burlington, MA, USA). Porcine liver was considered as a tissue model for

Biomedical Optics EXPRESS

the simulation study. A 3D geometry consisted of two parts: liver tissue and DA. The tissue was built in a cubic shape. The physical dimension of the tissue was $30 \times 30 \times 30$ mm^3. The DA had a core diameter of 600 μm and was vertically situated inside the tissue. The fabricated active length of the DA was 10 mm and protected by a cylindrical glass cap (i.e., outer diameter = 1.4 mm, thickness = 0.2 mm). A 0.2-mm gap between the DA and the glass cap was filled with air (Fig. 1(a)), and the DA surface made full contact with the tissue. The liver tissue was assumed to be homogenous and isotropic for the simulation, as shown in Table 1.

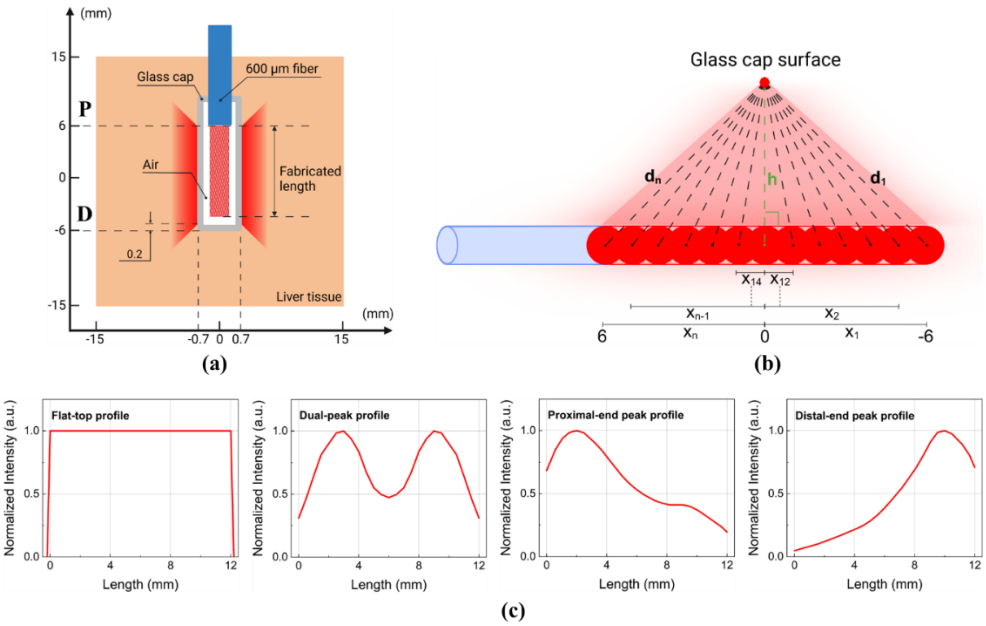

Fig. 1. Geometry for numerical simulations: (a) position of diffusing applicator in liver tissue (30×30×30 mm^3), (b) multiple point sources along applicator, and (c) four different emission profiles used for simulations (P: proximal end and D: distal end).

Table 1. Physical parameters of liver tissue at 980 nm used for thermal damage simulation

Wavelength	Absorption coefficient (μ_a, mm^{-1})	Scattering coefficient (μ_s, mm^{-1})	Anisotropy factor (g)	Frequency factor (A_f, 1/s)	Activation energy (E_a, J/mol)	Universal gas constant (R, J/mol·K)	Ref
980 nm	0.064	4.72	0.93	5.5×10^{41}	2.77×10^5	8.314	[18]

The previous studies tested DA-delivered 980 nm laser wavelength at the power levels of 5~30 W for 60 s or longer (in continuous mode) and showed a good ablation capacity in terms of low complications and tumor recurrence [34–40]. Specifically, the DA-based ILT with 980 nm at 5 W for 75 s presented the well-suited treatment with deep ablation of localized PC [41]. As a result, the current study decided to employ the condition of 5 W for 60 s to simultaneously maintain treatment efficiency and prevent the hazards of the long irradiation time of the high power laser under laboratory conditions. Since the main parameter for light propagation is fluence rate, DA was discretized as a sum of n-light point source [42,43]. At a distance from the DA surface, the fluence rate $\phi(d)$ (W/mm^2) from the DA was thus the sum of n light sources, as follows [42,43]:

$$\phi(d) = \sum_1^n \phi(d_n) = \sum_1^n \frac{P}{L_{DA}} \cdot \frac{3\mu_s'}{4\pi d_n} \cdot e^{-d_n \mu_{eff}} \cdot \Delta L \quad (1)$$

Biomedical Optics EXPRESS

where $n = \frac{L_{DA}}{\Delta L}$, P = power of source (W), L_{DA} = DA length (mm), ΔL = constant step length of discretization between two continuous point sources (mm), μ_s'= reduced scattering coefficient (mm^{-1}) = $(1\text{-}g)\mu_s$, μ_{eff} = effective attenuation coefficient (mm^{-1}) = $\sqrt{3\mu_a(\mu_a + \mu_s')}$, μ_a = absorption coefficient (mm^{-1}), and d_n = distance between the n-th point of the point light source and the observing point (mm) = $\sqrt{x_n^2 + h^2}$(x_n mm, n: odd number). The $\frac{n-1}{2}$ point was set as the coordinate origin at the middle of the L_{DA} [44]. x_n was the distance between the $\frac{n-1}{2}$ point source and other point sources. h was the perpendicular distance from the point source to the glass cap surface (Fig. 1(b)), representing the radius of glass cap. Table 2 presents all the values used for the simulated variables.

Table 2. Variables used in diffusing applicator simulation

Variable	Value	Unit
P	5	W
$L_{diffuser\ length}$	12	mm
ΔL	0.5	mm
n	25	
h	0.7	mm
x_n	6–0.5×(n-1)	mm

Numerical simulations evaluated four different beam profiles (Fig. 1(c)). Among them, a flat-top beam profile (top left in Fig. 1(c)) was simulated as a reference (i.e., flat-top beam profile) [31,45]. All the profiles had the equivalent laser power. The incident laser light from DA was assumed to have a uniform distribution on the glass cap surface along the radial direction. No light absorption by the air and the glass cap was assumed. The thermal response of tissue was described by using the Pennes bioheat transfer equation with Beer's law as below [18,45,46]:

$$\rho c \cdot \frac{\partial T(r,z,t)}{\partial t} = \nabla \cdot (k \nabla T(r,z,t)) + Q_{blood} + Q_{met} + Q_{ext} \tag{2}$$

where k (W/m·K) is thermal conductivity, ρ (kg/m^3) is density, c (J/kg·K) is specific heat, and T (K) is the local tissue temperature. The initial tissue temperature was set at 20 °C. Q_{blood} (W/m^3) and Q_{met} (W/m^3) express the internal heat source in blood perfusion and the metabolic heat generation per unit volume, respectively. For simplicity, both Q_{blood} and Q_{met} were neglected (i.e., $Q_{blood} = 0$ and $Q_{met} = 0$) owing to in vitro conditions. Q_{ext} (W/m^3) is the heat source induced by the laser light as calculated by:

$$Q_{ext} = \mu_a \times \phi(d) \tag{3}$$

The porcine liver tissue's thermal properties (i.e., k (W/m·K), ρ (kg/m^3), and c (J/kg·K)) were determined by a function of temperature T in the range of 20-100 °C during laser irradiation [18,46–48]:

$$k(T) = 0.419 \cdot [0.133 + 1.36 \cdot k_k(T) \cdot w] \tag{4}$$

$$\rho(T) = 1000 \cdot [1.3 - 0.3 \cdot k\rho(T) \cdot w] \tag{5}$$

$$c(T) = 4190 \cdot [0.37 + 0.63 \cdot k_c(T) \cdot w] \tag{6}$$

where w is the mass percentage of water in the tissue (i.e., $w = 69\%$ for liver tissue). The values of $k_k(T)$, $k_\rho(T)$, and $k_c(T)$ are temperature-dependent for density, specific heat, and thermal

Biomedical Optics EXPRESS

conductivity of water, respectively, as shown below:

$$k_k(T) = 1 + 1.78 \times 10^{-3} \cdot (T - 20°C) \tag{7}$$

$$k_\rho(T) = 1 - 4.98 \times 10^{-4} \cdot (T - 20°C) \tag{8}$$

$$k_c(T) = 1 + 1.016 \times 10^{-4} \cdot (T - 20°C) \tag{9}$$

Table 3 presents all the thermal properties of both air and glass used for the current simulations.

Table 3. Thermal properties of materials used in numerical simulation

Property	k (W/m·K)	ρ (kg/m^3)	c (J/kg·K)	Reference
Glass	1.3	2200	820	[18]
Air	0.0257	1.205	1005	[18]

The degree of thermal damage was quantified by using an Arrhenius damage integral equation, which is exponentially dependent on the temperature and the exposure time as shown:

$$\Omega(r, \tau) = A_f \cdot \int_0^\tau \exp\left[\frac{-E_a}{RT(r,t)}\right] dt \tag{10}$$

where Ω is dimensionless, A_f (1/s) is the frequency factor, E_a (J/mol) is the denaturation activation energy, R (J/mol·K) is the universal gas constant of 8.314, T (K) is the absolute temperature in tissue, and τ (s) is the laser irradiation time ($\tau = 60$ s for current damage model). $\Omega = 1$ (i.e., $\log(\Omega) = 0$) demonstrates the irreversible thermal damage of the tissue when the tissue temperature increases over 60 °C [47,49–51]. Table 1 lists the optical properties of the liver at 980 nm.

2.2. Device preparation

A CO2 laser system was employed to micro-machine the surface of optical fiber. Multimode optical fibers with a 600-μm core diameter (FP600URT, Thorlabs Inc., Newton, New Jersey, USA) were used to fabricate DAs with various emission profiles (i.e., dual-peak, proximal-end peak, and distal-end peak emission profiles) (Fig. 1(c)). Proximal-end and distal-end peak profiles were commonly found in the fabricated DAs, as observed in [18,32]. Although DAs were fabricated by the CO_2 laser processing technique [32], DAs still transmitted the forward light at the DA distal end [32,52,53], which resulted in a non-uniform light distribution in the targeted tissue. Due to the challenge of achieving the uniform emission [18,31], the flat-top profile was only used for numerical analysis and comparison. The DAs were fabricated to have an active length of 10 mm ($L_{cutting}$ = 10 mm). With the same $L_{cutting}$ value, the intensity peak position could be controlled by cutting depth. The deep cutting depth yielded the intensity peak at the right-skewed positions (i.e., proximal-end peak profile). On the other hand, the shallow cutting depth yielded the intensity peak at the left-skewed positions (i.e., distal-end peak profile). Combination of both deep and shallow cutting depth at respective proximal-end and distal-end directions produced the dual-peak profile. After the fabrication, the DAs were sealed with a customized glass cap (outer diameter = 1.4 mm, length = 15 mm) by using an epoxy. The distance between DA tips and the top point of glass cap was 2 mm (L_{gap} = 2 mm). Before experiments, HeNe laser light (λ=632 nm, Thorlabs Inc., Newton, New Jersey, USA), in conjunction with a digital camera (D5100, Nikon Corp., Tokyo, Japan) was utilized to visualize and confirm the spatial emissions of the DAs. The fabricated DA surface was captured by using a digital microscope (VHX-7100, Keyence corp., Gyeonggi-do, South Korea). The longitudinal emission profile was measured by employing a customized goniometric system (PD-300-3W, Ophir, Jerusalem, Israel) [32] at multiple distances (i.e., d = 0.5, 1, 3, 5, 10 mm) from the DA surface to a sensor. For dual-peak profile, the intensity difference between two intensity peaks was ΔI.

Biomedical Optics EXPRESS

2.3. Ex vivo tests

For ex vivo tests, liver tissues were procured from a local slaughterhouse and stored at 4 °C to prevent any structural deformation and dehydration. Each tissue sample was cut into $30 \times 30 \times 30$ mm^3 and maintained at the room temperature (20 °C). A 17 G needle (1.47 mm outer diameter, 38 mm length, Sungshim Medical Co.,Ltd., Bucheon, Gyeonggi, South Korea) was used to make a hole in the tissue to insert a DA prior to irradiation. A 980-nm diode laser system (EsoLight Z360, TeCure Inc., Busan, Republic) in conjunction with the DAs was utilized to coagulate the liver tissues interstitially. The conditions of 5 W and 60 s were selected for the applied power and irradiation time, respectively, for ILT. After each ILT, the surface of glass cap was cleaned to minimize any experimental error. Post-experimentally, each tissue was cut along the DA axis to show the longitudinal sections of the tissue (Fig. 2(a)).

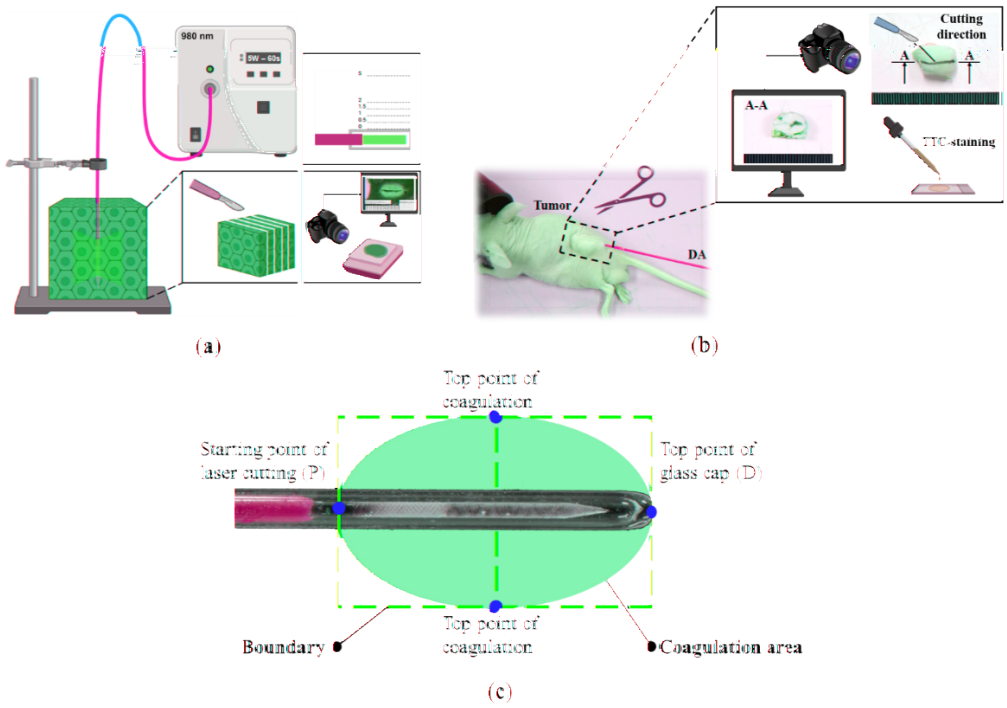

Fig. 2. Schematics of experimental set-ups: (a) ex vivo test using porcine liver tissue, (b) in vivo test in tumor-bearing mice, and (c) rectangular boundary determination. Note that the applied wavelength was 980 nm and the treatment condition was 5 W for 60 s.

2.4. In vivo tests

For in vivo tests, tumor models were developed by seeding DU145 Human prostate cancer cells to a BALB/c Nude male mouse (five weeks old; 20-25 g weight). A total of 12 mice were procured from Hana Biotech (Suwon, Korea) and divided into four groups (i.e., sham, dual-peak, proximal-end peak, and distal-end peak). DU145 from the Korean cell line bank was cultured in Dulbecco's modified Eagle's Medium (DMEM, Corning, NY) with 10% fetal bovine serum (FBS, Corning, NY) and 1% antibiotic-antimycotic (Gibco, Grand Island, NY). The cultured cells were incubated at 37 °C with 5% CO_2 and injected into the back side of each mouse by 7.0×10^6. ILT was conducted on the tumor tissue at 5 W for 60 s. After the ILT, the animals were anesthetized by using a respiratory anesthesia system (Classic T3, SurgiVet, Minneapolis, MN, USA) with 3% isoflurane (Terrell isoflurane, Piramal Critica 1 Care, Bethlehem, PA, USA)

Biomedical Optics EXPRESS

in oxygen (0.6 L/min). As with ex vivo experiments, the surface of glass cap was cleaned to minimize any experimental error after each ILT. The animal study of the current research was conducted under the approval of Institutional Animal Care at Pukyong National University (permit number: PKNUIACUC-2023-30).

All animals were euthanized 2 hours after ILT, and the entire tumor tissues were harvested from the animals. To evaluate thermal damaged extent along DA, 2,3,5-triphenyltetrazolium chloride (TTC) staining was conducted. For the TTC staining, the extracted tissues were sliced into 2 mm sections (longitudinally) and incubated in 1% TTC solution for 30 min without light. The sliced tissues were washed by using PBS for three times and fixed in 10% neutral formalin. The TTC stained tissues were captured by using a digital camera (D5100, Nikon, Tokyo, Japan) (Fig. 2(b)).

2.5. Geometric evaluations

The proximal (P)-/distal (D)-end positions of treatment devices can be utilized to determine the extent of thermal coagulation inside tissue in in vivo experiments [54,55]. For both ex vivo and in vivo tests, coagulation areas were bisected by the length of proximal-/distal end positions L_{PD} ($L_{PD} = L_{cutting} + L_{gap} = 12$ mm). The P-D length was defined by the active length of the glass cap-sealed DA (Fig. 2(c)). The P position was the starting position of laser cutting on the DA surface whereas the D position was the top point of the glass cap. The coagulation areas from the experiments were captured by using a digital camera. The coagulation areas were defined as the discolored regions (i.e., tan color for ex vivo [56] and whitish color for in vivo [57]) in the treated tissue. Each coagulation boundary was marked by a dashed line (Fig. 6: dashed yellow line, and Fig. 7: dashed black line). The longitudinal sections were analyzed by Image J software (Version 1.53 t, National Institute of the Health, Bethesda, MD, USA) for dimensional measurement. Based on P-D positions and dashed lines, a rectangular boundary (dashed red line) was created to identify the extent of thermal coagulation. The length of the rectangular boundaries were tangent to the cross-sectional direction of the coagulation at the top two points on the opposite sides. The rectangular length was equal to the L_{PD} value. The width of the rectangular boundaries were established by passing through the P-D points (Fig. 2(c)). To identify the geometric uniformity of thermal coagulation, two geometric factors were considered: symmetry ratio (SR) and filling-area ratio (FR). SR was defined as the ratio of the smaller coagulation portion (S_{s-half}) to the larger coagulation portion (S_{b-half}) ($SR = S_{s-half}/S_{b-half} \leq 1$). S_{s-half} and S_{b-half} portions were determined by dividing the length of boundary into equal halves as shown in Fig. 6. FR was defined as the ratio of the coagulation area ($S_{coagulation}$) to the rectangular boundary area ($S_{rectangle}$) (Fig. 6, $FR = S_{coagulation}/S_{rectangle} \leq 1$). Inkscape software (version 0.92.4, Software Freedom Conservancy Inc., Brooklyn, NY, USA) and SOLIDWORKS 2016 software (Dassault Systumes SOLIDWORKS Corp., Waltham, Massachusetts, USA) were implemented to estimate the rectangular boundary areas.

2.6. Statistical analysis

All the data were presented as the mean ± standard deviation, and SPSS program (version 20, SPSS Inc., Chicago, IL, USA) was used for statistical analysis. Mann–Whitney U tests were chosen to evaluate any statistical difference between two groups. Statistical significance was considered as $p < 0.05$.

3. Results

Figure 3 characterizes various emission profiles measured from the fabricated DAs. The normalized intensities (a.u.) were measured from the fabricated DAs. In Fig. 3(a) (top), the two peaks occurred approximately at 3 and 9 mm along L_{PD}, respectively. The ΔI value was 8%. The intensity dropped at 6 mm from the DA tip and yielded a 53% lower intensity than the peak

Biomedical Optics EXPRESS

intensity. Comparing with a dual-peak profile, the highest peak position of proximal-/distal-end peak profiles occurred at approximately 2 and 10 mm, respectively (Figs. 3(b) and 3(c); top). Figure 3 (bottom) depicts that all the tips of DAs were etched into approximately a 25° conical angle, as proposed in [32]. The intensity peak appeared at P position when the cutting depth was deeper (Figs. 3(a) and 3(b); bottom) whereas the intensity peak occurred at D position when the cutting depth was shallower (Fig. 3(c); bottom). In turn, the position of the intensity peak could be contingent of the extent of the cutting depth.

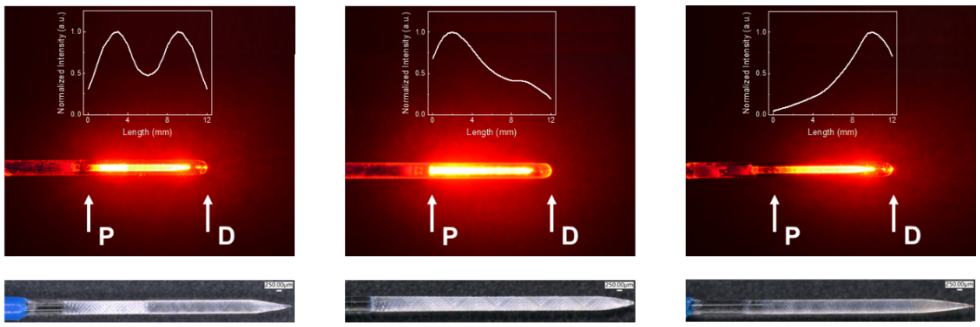

Fig. 3. Characterization of various emission profiles measured from the fabricated DAs: (a) dual-peak profile, (b) proximal-end peak profile, and (c) distal-end peak profile. The top images show He-Ne light distributions from each diffusing applicator, and the bottom images are the corresponding microscopic images (scale bar = 250 μm). The inlets (in top images) represent the beam profiles measured between proximal (P) and distal (D) ends.

Figure 4 depicts spatio-temperature developments at the interface between tissue and glass cap after irradiation at 5 W for 60 s with various emission profiles (top images). The red boundaries represent the coagulation threshold (i.e., 60 °C) for irreversible tissue denaturation. Both flat-top and dual-peak profiles had symmetry and elongated temperature distributions along the DA. On the other hand, proximal-end and distal-end peak profiles generated asymmetry (pear-shaped) temperature distributions. The bottom images in Fig. 4 exhibit the temporal developments of the cross-sectional temperature acquired from the dashed lines in the middle position of the top images. Regardless of emission profiles, the temperature increased with the irradiation time. In Fig. 4(a), the maximum temperature of a flat-top profile was maintained at the middle of L_{PD} and showed the uniform coagulation characterized by an elliptical shape along the L_{PD}. In Fig. 4(b), the temperature difference (ΔT) between the temperature at the position of intensity peak and one at the position where intensity dropped (in dual-peak profile) decreased over the irradiation time (i.e., ~ 4 °C at 5 s, ~2 °C at 30 s, and ~0.7 °C at 60 s). Thus, ΔT gradually became indistinguishable as the irradiation time increased. Moreover, the highest temperature tended to appear in the middle of the simulation model (i.e., 15 mm position) over time as ΔT decreased. In Figs. 4(c) and 4(d), the maximum temperatures of both proximal-end peak and distal-end peak profiles were associated with the right-skewed and left-skewed distribution from the middle of simulation model (i.e., 12 and 18 mm position, respectively) and caused the asymmetry of the temperature development over time. The flat-top, dual-peak, and proximal-end peak profiles yielded comparable maximum temperatures (i.e., 87, 84, and 86 °C, respectively). However, the distal-end peak profile created ~15% higher maximum temperature than the other profiles. Similarly, both flat-top and dual-peak profiles had uniform temperature distributions, while both the proximal-end and distal-end emissions accompanied asymmetry ones. It was noted that the

Biomedical Optics EXPRESS

dual-peak emission profile had a relatively flat and wide distribution of the maximum temperature after sufficient time.

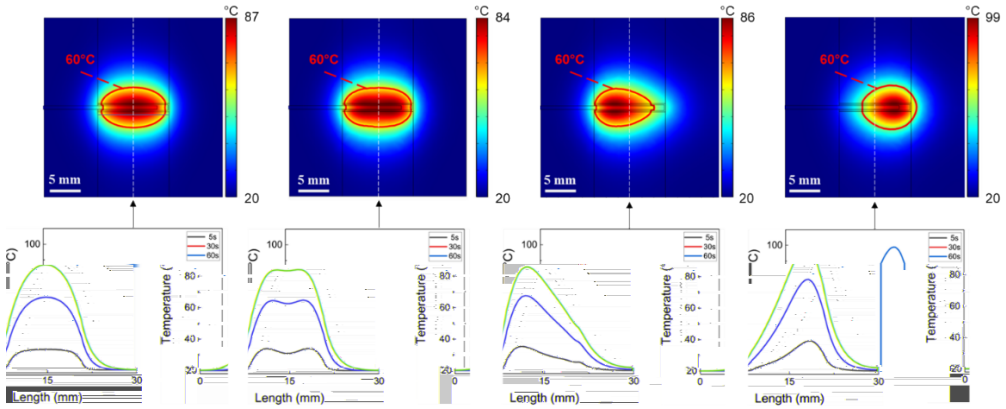

Fig. 4. Spatio-temporal developments of temperature acquired from numerical simulations at 0 mm (interface between tissue and glass cap) measured at various irradiation times of 5, 30 and 60 s: (a) flat-top profile, (b) dual-peak profile, (c) proximal-end peak profile, and (d) distal-end peak profile. The top images show the spatial distributions of the temperature developed in tissue after 60-s irradiation. The bottom images are the cross-sectional temperature profiles at various irradiation times.

Figure 5 displays temperature elevations at various tissue depths from the surface of DAs (tissue depth: d = 0, 0.5, 1, 1.5, 2, and 5 mm) after irradiation for 60 s. According to Fig. 5(a), for the flat-top profile, the highest temperature point was maintained at the center of simulation model (i.e., 15 mm position), regardless of d values during 60-s irradiation. In case of the dual-peak profile (Fig. 5(b)), the highest temperature occurred in the middle of the DA as shown similarly in Fig. 4(b). Additionally, the positions of two highest temperature points were indistinct after d > 1 mm. Therefore, the temperature development from the dual-peak profile became equivalent to that of the flat-top profile with increasing d. In Fig. 5(c), the highest temperature from the proximal-end peak profile at each d value was similar to that of the flat-top profile. Nevertheless, the temperature distribution from the proximal-end peak profile was more right-skewed than that of the flat-top profile. The similar tendency of the skewed temperature distribution (left-skewed) was observed in the distal-end peak profile (Fig. 5(d)). When the d value increased, the highest temperature points of both proximal-/distal-end peak profiles tended to displace toward the middle of L_{PD}, but the position displacement was insignificant after 60 s (i.e., from 12 mm and 18 mm when d = 0 mm to 13 mm and 17 mm when d = 5 mm, respectively, in simulation models). The temperature distribution of the dual-peak profile could be more equivalent to that of flat-top profile at 5 mm tissue depths.

Figure 6 compares the extent of thermal coagulation between simulations and ex vivo porcine liver tissue experiments after 60-s irradiation. The boundary of each coagulation area was determined by yellow dashed lines, as shown in Figs. 6(a) and 6(b). In both Figs. 6(a) and 6(b), the coagulation area from the dual-peak profile reflected the elliptical shape, whereas the other profiles (proximal-/distal-end profiles) were associated with the right-/ left-skewed coagulation shapes, respectively. The rectangular boundary was used to evaluate the coagulation extent. Figures 6(c) and 6(d) present the quantitative comparisons of coagulation extents inside the P-D boundary. In Fig. 6(c), the dual-peak profile yielded an equal extent of coagulation on both P-D sides and more uniform extent of coagulation than those of the proximal-/distal end peak profiles (i.e., $SR_{DP} = 0.92 \pm 0.06$, $SR_{PEP} = 0.7 \pm 0.1$, and $SR_{DEP} = 0.19 \pm 0.1$, $^{*}p < 0.01$, respectively).

Biomedical Optics EXPRESS

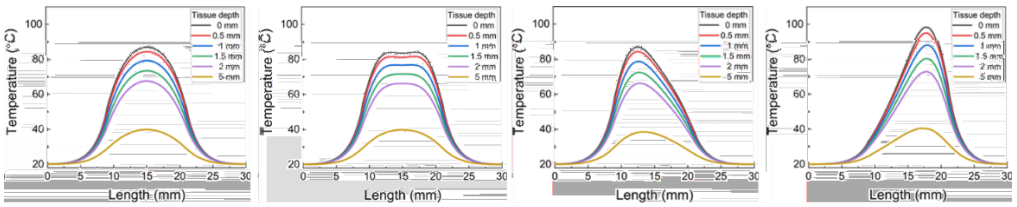

Fig. 5. Temperature distributions at various tissue depths acquired from numerical simulations after 60-s irradiations by (a) flat-top profile, (b) dual-peak profile, (c) proximal-end peak profile, and (d) distal-end peak profile. Note that the measured tissue depths ranged from 0 mm to 5 mm away from the applicator surface. (tissue depth: d = 0, 0.5, 1, 1.5, 2, and 5 mm).

In Fig. 6(d), the dual-peak profile resulted in the largest extent of the coagulation within the rectangular boundary (i.e., FR = 0.77 for simulation and FR = 0.86 ± 0.03 for experiment). The dual-peak profile created a larger extent of the coagulation than the proximal-end peak profile did ($FR_{PEP} = 0.7 \pm 0.1$, $^{**}p < 0.01$) by about 1.2 times and the distal-end peak profile ($FR_{DEP} = 0.6 \pm 0.08$, $^{\#\#}p = 0.002$) by about 1.4 times experimentally. The same trends of SR and FR comparisons were observed in the numerical simulations. Figure 6 shows that the dual-peak profile produced an equivalent extent of coagulation (~90%), compared to that of the flat-top profile (i.e., for simulation: $SR_{FP} = 0.98$, $FR_{FP} = 0.69$, $SR_{DP} = 0.97$, $FR_{DP} = 0.77$ and for experiment: $SR_{DP} = 0.92 \pm 0.06$, $FR_{DP} = 0.86 \pm 0.03$) and demonstrated a more uniform extent of thermal coagulation than those of the proximal-/distal end-peak profiles.

Figure 7 describes the extent of thermal coagulation created by three fabricated DAs in prostate tumor from in vivo experiments. A black dashed line was drawn to separate the boundaries of thermally-injured and normal areas (Fig. 7(a)). White areas indicated thermal coagulation areas whereas red areas indicated the normal areas. Sham-controlled models showed no thermally-injured areas upon DA insertion. Overall, the comparison of SR and FR factors among the profiles (Fig. 7(b)) followed the same trend as shown in Figs. 6(c) and 6(d). Similar to Fig. 6(c), the SR value of the dual-peak profile was higher than that of the proximal-/distal-end profiles (i.e., $SR_{DP} = 0.88 \pm 0.03$, $SR_{PEP} = 0.66 \pm 0.04$, and $SR_{DEP} = 0.25 \pm 0.03$; $p < 0.01$ respectively). The dual-peak profile exhibited a higher FR value ($FR_{DP} = 0.75 \pm 0.03$) than the proximal-end peak profile ($FR_{PEP} = 0.58 \pm 0.04$) by 1.3 times and the distal-end peak profile ($FR_{DEP} = 0.55 \pm 0.04$) by 1.4 times. The dual-peak profile could yield the extent of the thermal coagulation equivalent to that of the flat-top profile as well as more uniform thermal coagulation than those of the proximal-/ distal-end peak profiles along the L_{DP}.

Biomedical Optics EXPRESS

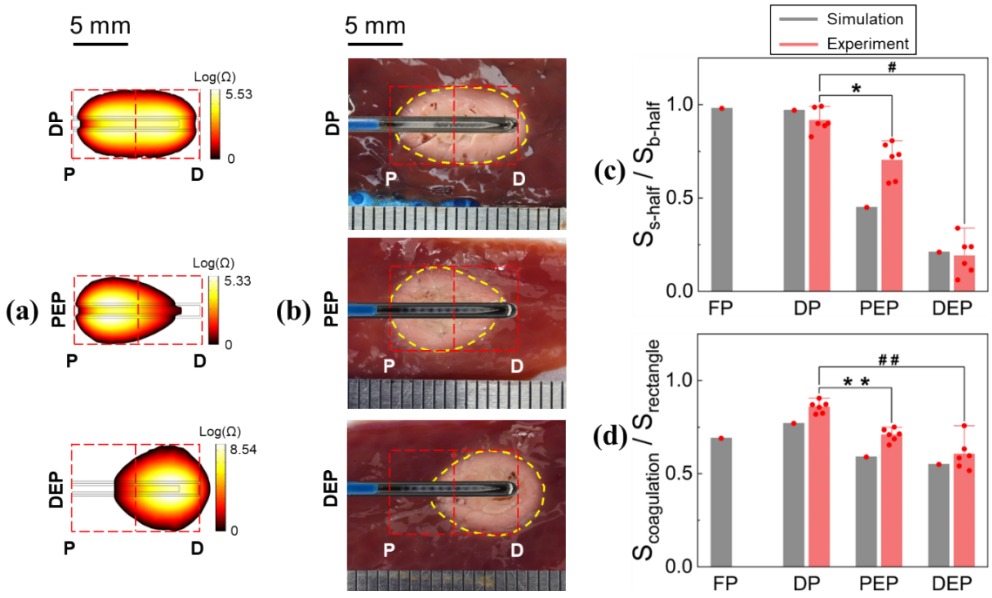

Fig. 6. Longitudinal views on thermal coagulation in ex vivo tissue: (a) numerical simulations, (b) ex vivo liver tests, and quantitative comparison of (c) symmetry ratio and (d) filling ratio (N = 6, *$p < 0.05$, #$p < 0.01$, **$p < 0.005$, ##$p < 0.001$). Note that the values on the color bar in Fig. 6(a) represent thermal damage and coagulation areas were measured from the red dashed rectangles. Red dots were raw datas. * and ** were the p-value of DP and PEP data sets. # and ## were the p-value of DP and DEP data sets. (FP = flat-top profile, DP = dual-peak, PEP = proximal-end peak profile, DEP = distal-end peak profile, P = proximal and D = distal ends, and S = coagulation area).

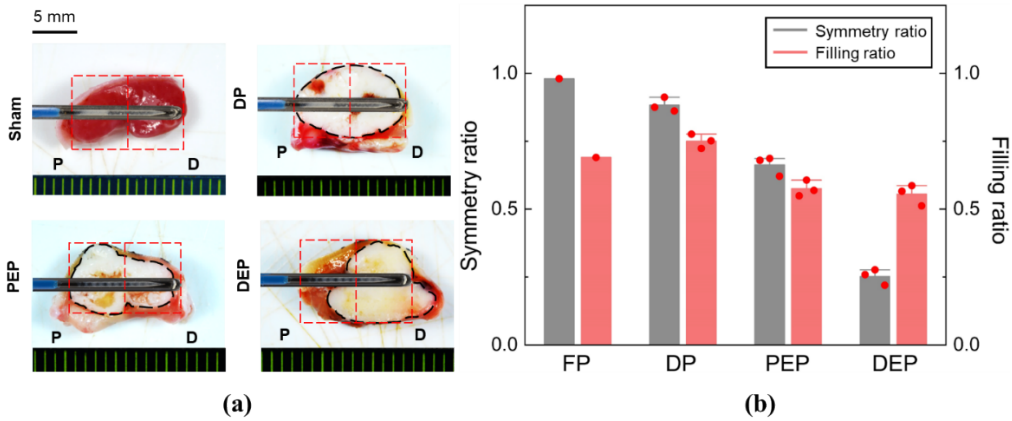

Fig. 7. Performance validation of various emission profiles in in vivo rat model: (a) TTC-stained longitudinal thermal coagulation and (b) quantitative comparison of symmetry and filling ratio. Red dots were raw datas. (DP = dual-peak, PEP = proximal-end peak profile, and DEP = distal-end peak profile; N = 3).

Biomedical Optics EXPRESS

4. Discussion

The uniform emission profiles produced by DAs is a desirable factor for controlling thermal area and attaining more predictable tissue responses during ILT [30,32,33,58,59]. Thus, the uniform profile can result in the accurate irradiation from DAs and minimize unfavorable thermal injury to the adjacent healthy tissue. The extent of coagulation inside the tissue depends on the spatial emission profile of DAs. The aim of this study was to investigate the effect of various emission profiles (i.e., dual-peak, proximal-end, and distal-end peak) on the performance of ILT for PC treatment numerically and experimentally. According to Figs. 6 and 7, the dual-peak profile could yield the equivalent extent of thermal coagulation to that of the flat-top profile and more uniform extent of thermal coagulation than those of proximal-/ distal-end peak profiles along the L_{DP}. The forward light still existed at the fiber tip position regardless of fabrication methods [32,52,58,60] and caused the excessive thermal coagulation during treatment. In this study, with dual-peak and distal-end peak profiles, the forward light caused coagulation over the rectangular boundary. With proximal-end peak profile, the forward light yielded a 37% higher symmetry ratio of experiment (~ 0.71) than that of simulation (~ 0.45; Fig. 6(c)). Thus, the D position was considered to be at the top point of the glass cap in this study due to the forward light (Fig. 3, top). From the equations (1-3), the local tissue temperature (T, °C) is proportional to the laser intensity, so the temperature development represents the laser intensity at specific position in tissue. The laser intensity is inversely proportional to the beam width (w) (i.e., $I \sim 1/w^2$ [61]). The beam width (w) of an arbitrary laser profile could be defined by $1/e^2$ (~0.135) intensity criterion [61], or a full width at half-maximum (FWHM) [62,63]. According to the $1/e^2$ criterion, the w value is defined as the distance between two points where the intensity level is ~ 0.135 of the peak intensity. In Fig. 1(c), while the w values of flat-top, dual-peak, and proximal-end peak profiles were 12 mm, that of distal-end peak profile was around 10 mm. Thus, distal-end peak profile yielded higher temperature than those of flat-top, dual-peak, and proximal-end peak profiles (Fig. 4).

In fact, the single peak formation of the dual-peak profile can be given by the partial differential heat conduction equation: $\partial T/\partial t = \alpha \times \partial^2 T/\partial x^2$ [64], for the explicit method, $[T_{(x,t+\Delta t)} - T_{(x,t)}]/\Delta t = \alpha \times [T_{(x+\Delta x,t)} - 2 \times T_{(x,t)} + T_{(x-\Delta x,t)}]/(\Delta x)^2$, where $T_{(x+\Delta x,t)}$ and $T_{(x-\Delta x,t)}$ are temperature of two considered intensity peaks, $T_{(x,t)}$ is temperature (K) at x (m), x is the midpoint position between two considered intensity peaks (m), t is irradiation time (s), Δt is irradiation time step (s), and $\alpha = k/\rho/c$ is thermal diffusivity ($m^2 s^{-1}$) (k, ρ, and c are from Eq. (2)). The equation explains the effect of heat flow on the temperature as the regions of high temperature cool down while the regions of low temperature heat up. Consequently, the two highest temperature from the dual-peak profile will form a single highest temperature gradually at the midpoint of light source length (L_{PD}) over time. In this study, $T_{(x+\Delta x,t)} - T_{(x-\Delta x,t)}$ was proportional to ΔI (intensity difference between two intensity peaks), $T_{(x,t+\Delta t)} - T_{(x,t)}$ was equal to ΔT (temperature difference in dual-peak profile between temperature at the position of intensity peak and one at the position where the intensity dropped), and Δx (mm) was the distance between the two highest temperatures (or intensity peaks). Due to the same experiment conditions during profile comparisons, three variables from the partial differential heat conduction equation (i.e., ΔI, ΔT, and Δx) influenced the heat flow effect. In Fig. 1(c), the two intensity peaks of the three profiles were considered at 2 mm and 10 mm of L_{PD}. The ΔI value of the dual-peak profile was 8%, whereas those of proximal-/distal-end peak profiles were 63% and 88% respectively. After 60-s irradiation, the dual-peak profile formed the uniform temperature distribution at the middle position of L_{PD}, while the proximal-/distal-end peak profiles respectively formed the right-/left-skewed temperature distribution (Figs. 4, 6, and 7). The similar effect of ΔI value was also seen in the previous studies [51,56,60]. The formed single intensity peaks became uniform with ΔI = 2% [51,60] and ΔI = 6% [56] after the 60-s irradiation. In contrast, the single intensity peaks forrmed the non-uniform distributions with ΔI = 25% (right-skewed) and 45% (left-skewed) in [32] and

Biomedical Optics EXPRESS

$\Delta I = 28\%$ (left-skewed) in [65]. Therefore, the low ΔI value can lead to the rapid formation of the uniform temperature distribution at the same Δx.

Figure 5(b) illustrates the effect of ΔT on temperature distribution. The ΔT value decreased incrementally with the tissue depth [31]. After 60-s irradiation, the ΔT decreased from 4 °C (at $d = 0$ mm) to 0.4 °C (at $d = 2$ mm). As a result, the dual-peak could yield an insignificant difference of temperature distribution, compared to that of flat-top profile when $d > 2$ mm. The relation between Δx and the temporal temperature development from the dual-peak profile within the tissues was evaluated in various studies [31,65,66]. The two highest intensity peaks became indistinguishable at $d = 1$, 1.9, 3.3, and 4.6 mm when $\Delta x = 2$, 3, 4, and 5 mm, respectively [31], $d = 10$ mm when $\Delta x = 20$ mm [65], and $d = 30$ mm when $\Delta x = 20$ mm [66]. According to the current study ($\Delta x = 8$ mm), the equivalent flat-top distribution appeared at $d = 5$ mm (Fig. 5(b)). In addition, the dual-peak profile was evaluated by comparing the measurement difference between the Fiber Bragg Grating (FBG) and thermocouple (TC) sensors (ΔT_{W-TC} - ΔT_{FBG}) [67] at $d = 9$ mm away from the DA center axis. At the different sensor positions along the active length of DA, the ΔT_{W-TC} - ΔT_{FBG} values were insignificant (i.e., 3.7 ± 0.7 °C, 3.5 ± 0.2 °C, 3.5 ± 0.1 °C, and 3.2 ± 0.3 °C for 0, 2, 4, and 6 mm from center of DA, respectively). Thus, the uniform temperature distribution from the dual-peak profile can be monitored at various tissue depths, based on the values of ΔT and Δx.

Although the current study compared the performance of various emission profiles for ILT of PC, experimental limitations still remain. The forward light leakage was associated with the fabrication method used in the current study (i.e., spiral-cutting on conical fiber tip by CO_2 laser) [18,32] as a few instances of the excessive thermal coagulation existed, as shown in Figs. 6(b) and 6(d). The minimization of the forward light leakage can be achieved by coating the reflective layers at the tip of the glass cap [32]. The two peaks at $d = 0$ mm also had the strongest intensities. To prevent the overtreatment induced by light intensity and thermal diffusion, the temporal development of the temperature in tissue layers close to the glass cap-tissue interface should be monitored [31]. The blackbody radiation is a promising temperature monitoring technique for addressing overheating issues [68]. The two intensity peaks could merge into a single intensity peak over time at a given value of d and low ΔI. Due to the inherent factors, such as blood perfusion [69], initial body temperature, and non-uniformity of cultured tissue [67,70], the comparison of SR and FR values were different between ex vivo and in vivo experiments (i.e., 4.5% and 12.8% for SR and FR, respectively). Additionally, both rat tumor size and DA insertion without a guiding device in the current study could restrict the accurate determination of the extent of thermal coagulation. Moreover, to prevent microcracking that affects profile redistribution, the mechanical strength testing of the dual-peak profile DA should be considered [71]. Pre-surgery imaging could provide data on tumor shape and size [72]. A capacity to have different light profiles suggests that clinicians may be able to select a specific profile for each determined tumor shape. Further in vivo models with diverse tumor sizes and different laser parameters (power, irradiation time) should be tested to warrant the efficacy and safety of the dual-peak emission profile for ILT of solid tumors.

5. Conclusion

The current study demonstrated the capacity to fabricate and the effect of various emission profiles from DAs on ILT of PC numerically and experimentally. Because of the symmetry emission profile, the dual-peak was able to yield larger and more predictable thermal coagulation in tissue. Further in vivo experiments with different tumor sizes will be conducted to warrant the performance of the dual-peak profile in terms of efficacy and safety of ILT for clinical translation.

Funding. National Research Foundation of Korea; Ministry of SMEs and Startups.

Biomedical Optics EXPRESS

Acknowledgements. This work was supported by the Technological Innovation R&D Program (RS-2024-00443980) funded by the Ministry of SMEs and Startups (MSS, Korea) and Basic Science Research Program through the National Research Foundation of Korea (NRF) funded by the Ministry of Education (RS-2021-NR060118).

Disclosures. The authors declare no conflicts of interest related to this article.

Data availability. Data underlying the results presented in this paper are not publicly available at this time but may be obtained from the authors upon reasonable request.

References

1. Á. Sánchez Iglesias, V. Morillo Macías, A. Picó Peris, *et al.*, "Prostate Region-Wise Imaging Biomarker Profiles for Risk Stratification and Biochemical Recurrence Prediction," Cancers **15**(16), 4163 (2023).
2. P. Posdzich, C. Darr, T. Hilser, *et al.*, "Metastatic Prostate Cancer—A Review of Current Treatment Options and Promising New Approaches," Cancers **15**(2), 461 (2023).
3. Z. Qin, D. Liu, Y. Zhang, *et al.*, "Inhibitory function of CDK12i combined with WEE1i on castration-resistant prostate cancer cells in vitro and in vivo," Oncologie **25**(6), 717 (2023).
4. L. Wang, B. Lu, M. He, *et al.*, "Prostate cancer incidence and mortality: global status and temporal trends in 89 countries from 2000 to 2019," Front. Public Health **10**, 811044 (2022).
5. H. Sung, S. Hassanipour-Azgomi, R. L. Siegel, *et al.*, "Global cancer statistics 2020: GLOBOCAN estimates of incidence and mortality worldwide for 36 cancers in 185 countries," Ca-Cancer J. Clin. **71**(3), 209–249 (2021).
6. S. Hassanipour-Azgomi, A. Mohammadian-Hafshejani, M. Ghoncheh, *et al.*, "Incidence and mortality of prostate cancer and their relationship with the Human Development Index worldwide," Prostate international **4**(3), 118–124 (2016).
7. M. Sekhoacha, K. Riet, P. Motloung, *et al.*, "Prostate cancer review: Genetics, diagnosis, treatment options, and alternative approaches," Molecules **27**(17), 5730 (2022).
8. J. Huang, E. O.-T. Chan, X. Liu, *et al.*, "Global trends of prostate cancer by age, and their associations with gross domestic product (GDP), human development index (HDI), smoking, and alcohol drinking," Clin. Genitourin. Cancer **21**(4), e261–e270.e50 (2023).
9. O. Bergengren, D. Silva, K. Matsoukas, *et al.*, "2022 Update on Prostate Cancer Epidemiology and Risk Factors—A Systematic Review," Eur. Urol. **84**(2), 191–206 (2023).
10. D. Silva and F. J. Alcorn, "A tale of two cancers: A current concise overview of breast and prostate cancer," Cancers **14**(12), 2954 (2022).
11. R. L. Siegel, K. D. Miller, N. S. Wagle, *et al.*, "Cancer statistics," Ca-Cancer J. Clin. **72**(1), 7–33 (2022).
12. Y. Zheng, S. X. Lin, S. Wu, *et al.*, "Clinicopathological characteristics of localized prostate cancer in younger men aged ≤ 50 years treated with radical prostatectomy in the PSA era: A systematic review and meta-analysis," Cancer Med. **9**(18), 6473–6484 (2020).
13. A. Bleyer, F. Spreafico, and R. Barr, "Prostate cancer in young men: An emerging young adult and older adolescent challenge," Cancer **126**(1), 46–57 (2020).
14. S. Kumari, N. Sharma, and S. V. Sahi, "Advances in cancer therapeutics: Conventional thermal therapy to nanotechnology-based photothermal therapy," Pharmaceutics **13**(8), 1174 (2021).
15. A. Van Luijtelaar, B. M. Greenwood, H. U. Ahmed, *et al.*, "Focal laser ablation as clinical treatment of prostate cancer: report from a Delphi consensus project," World J. Urol. **37**(10), 2147–2153 (2019).
16. R. Liu, L. Yaqiong, M. Bing, *et al.*, "Focal Ablation Therapy for Prostate Cancer: A Literature Review," Advanced Ultrasound in Diagnosis and Therapy **4**(4), 308–314 (2020).
17. M. Ahdoot, A. H. Lebastchi, B. Turkbey, *et al.*, "Contemporary treatments in prostate cancer focal therapy," Curr. Opin. Oncol. **31**(3), 200–206 (2019).
18. T. H. Nguyen, S. Park, K. K. Hlaing, *et al.*, "Temperature feedback-controlled photothermal treatment with diffusing applicator: theoretical and experimental evaluations," Biomed. Opt. Express **7**(5), 1932–1947 (2016).
19. Q. Xue, J. Zhang, J. Jiao, *et al.*, "Photodynamic therapy for prostate cancer: Recent advances, challenges and opportunities," Front. Oncol. **12**, 980239 (2022).
20. P. Tombesi, F. D. Vece, and S. Sartori, "Radiofrequency, microwave, and laser ablation of liver tumors: time to move toward a tailored ablation technique?" Hepatoma Res. **1**(2), 52–57 (2015).
21. F. Izzo, V. Granata, R. Grassi, *et al.*, "Radiofrequency ablation and microwave ablation in liver tumors: an update," The oncologist **24**(10), e990–e1005 (2019).
22. E. De Vita, D. Lo Presti, C. Massaroni, *et al.*, "A review on radiofrequency, laser, and microwave ablations and their thermal monitoring through fiber Bragg gratings," iScience **26**(11), 108260 (2023).
23. R. Geoghegan, G. ter Haar, K. Nightingale, *et al.*, "Methods of monitoring thermal ablation of soft tissue tumors–A comprehensive review," Med. Phys. **49**(2), 769–791 (2022).
24. J. H. Correia, José A. Rodrigues, S. Pimenta, *et al.*, "Photodynamic therapy review: principles, photosensitizers, applications, and future directions," Pharmaceutics **13**(9), 1332 (2021).
25. J. Park, Y.-K. Lee, I.-K. Park, *et al.*, "Current limitations and recent progress in nanomedicine for clinically available photodynamic therapy," Biomedicines **9**(1), 85 (2021).
26. G. Gunaydin, M. E. Gedik, and S. Ayan, "Photodynamic therapy—current limitations and novel approaches," Front. Chem. **9**, 691697 (2021).

Biomedical Optics EXPRESS

27. C. Yakkala, A. Denys, L. Kandalaft, *et al.*, "Cryoablation and immunotherapy of cancer," Curr. Opin. Biotechnol. **65**, 60–64 (2020).
28. K. Kwak, B. Yu, R. J. Lewandowski, *et al.*, "Recent progress in cryoablation cancer therapy and nanoparticles mediated cryoablation," Theranostics **12**(5), 2175–2204 (2022).
29. J. S. Fainberg, B. Al Hussein Al Awamlh, A. P. DeRosa, *et al.*, "A systematic review of outcomes after thermal and nonthermal partial prostate ablation," Prostate International **9**(4), 169–175 (2021).
30. M. D. Stringasci, T. C. Fortunato, L. T. Moriyama, *et al.*, "Interstitial PDT using diffuser fiber—investigation in phantom and in vivo models," Lasers Med. Sci. **32**(5), 1009–1016 (2017).
31. S. Ströbl, M. Domke, A. Rühm, *et al.*, "Investigation of non-uniformly emitting optical fiber diffusers on the light distribution in tissue," Biomed. Opt. Express **11**(7), 3601–3617 (2020).
32. V. G. Truong, S. Park, and H. W. Kang, "Spatial effect of conical angle on optical-thermal distribution for circumferential photocoagulation," Biomed. Opt. Express **8**(12), 5663–5674 (2017).
33. H. Stepp and R. Sroka, "Simple Characterization of Cylindrical Diffuser Fibers With a Fluorescent Layer," Lasers Surg. Med. **56**(6), 597–605 (2024).
34. W. G. Brisbane, S. Natarajan, A. Priester, *et al.*, "Focal laser ablation of prostate cancer: an office procedure," JoVE **30**(169), e61984 (2021).
35. E. Schena, P. Saccomandi, and Y. Fong, "Laser ablation for cancer: past, present and future," J. Funct. Biomater. **8**(2), 19 (2017).
36. H. Wenger, A. Yousuf, A. Oto, *et al.*, "Laser ablation as focal therapy for prostate cancer," Curr. Opin. Neurol. **24**(3), 236–240 (2014).
37. R. Geoghegan, A. Santamaria, A. Priester, *et al.*, "A tissue-mimicking prostate phantom for 980 nm laser interstitial thermal therapy," Int. J. Hyperthermia **36**(1), 992–1001 (2019).
38. C. L. Li, C. J. Fisher, B. C. Wilson, *et al.*, "Preclinical evaluation of a clinical prototype transrectal diffuse optical tomography system for monitoring photothermal therapy of focal prostate cancer," J. Biomed. Opt. **27**(02), 026001 (2022).
39. M. H. Mithani, S. E. Khalid, S. A. Khan, *et al.*, "Outcome of 980 nm diode laser vaporization for benign prostatic hyperplasia: A prospective study," Investig. Clin. Urol. **59**(6), 392–398 (2018).
40. H. Miyazaki, P. Colin, S. Kato, *et al.*, *Early experiences of contact laser vaporization of the prostate using the 980 nm high power diode laser for benign prostatic hyperplasia*, LUTS: Lower Urinary Tract Symptoms, 2018. 10(3): p. 242–246.
41. P. Colin, P. Nevoux, M. Marqa, *et al.*, "Focal laser interstitial thermotherapy (LITT) at 980 nm for prostate cancer: treatment feasibility in Dunning R3327-AT2 rat prostate tumour," BJU International **109**(3), 452–458 (2012).
42. C. Dupont, A.-S. Vignion, S. Mordon, *et al.*, "Photodynamic therapy for glioblastoma: A preliminary approach for practical application of light propagation models," Lasers Surg. Med. **50**(5), 523–534 (2018).
43. F.S. Ismael, H. Amasha, and W. Bachir, "Optimized cylindrical diffuser powers for interstitial PDT breast cancer treatment planning: a simulation study," BioMed Res. Int. **2020**, 1–11 (2020).
44. X. Zhou, K. Jin, S. Qiu, *et al.*, "Comparative effectiveness of radiotherapy versus focal laser ablation in patients with low and intermediate risk localized prostate cancer," Sci. Rep. **10**(1), 9112 (2020).
45. T. H. Nguyen, Y.-h. Rhee, J.-c. Ahn, *et al.*, "Circumferential irradiation for interstitial coagulation of urethral stricture," Opt. Express **23**(16), 20829–20840 (2015).
46. S. Lim, V. G. Truong, and H. W. Kang, "Impact of residual air trap in balloon on laser treatment of tubular tissue," Lasers Surg. Med. **54**(5), 767–778 (2022).
47. S. Jiang and X. Zhang, "Effects of dynamic changes of tissue properties during laser-induced interstitial thermotherapy (LITT)," Lasers Med. Sci. **19**(4), 197–202 (2005).
48. K. S. Shibib, M. A. Munshid, and H. A. Lateef, "The effect of laser power, blood perfusion, thermal and optical properties of human liver tissue on thermal damage in LITT," Lasers Med. Sci. **32**(9), 2039–2046 (2017).
49. A. Mohammadi, L. Bianchi, S. Asadi, *et al.*, "Measurement of ex vivo liver, brain and pancreas thermal properties as function of temperature," Sensors **21**(12), 4236 (2021).
50. J. Bak, H. J. Pyo, J. M. Choi, *et al.*, "Dependence of photothermal responses on wavelengths," J. Korean Phys. Soc. **74**(3), 224–230 (2019).
51. N. T. Pham, S. L. Lee, S. Park, *et al.*, "Real-time temperature monitoring with fiber Bragg grating sensor during diffuser-assisted laser-induced interstitial thermotherapy," J. Biomed. Opt. **22**(4), 045008 (2017).
52. J.-S. Park, S. Jeong, D. H. Lee, *et al.*, "The use of a 532-nm laser fitted with a balloon and a cylindrical light diffuser to treat benign biliary stricture: a pilot study," Lasers Med. Sci. **36**(1), 25–31 (2021).
53. J. Köcher, V. Knappe, and M. Schwagmeier, "Internal structuring of silica glass fibers: Requirements for scattered light applicators for the usability in medicine," Photonics Lasers Med. **5**(1), 57–67 (2016).
54. V. K. Sharma, "Ablation of Barrett's esophagus using the HALO radiofrequency ablation system," Techniques in Gastrointestinal Endoscopy **12**(1), 26–34 (2010).
55. V. G. Truong, S. Jeong, J.-S. Park, *et al.*, "Endoscopic ultrasound (EUS)-guided cylindrical interstitial laser ablation (CILA) on in vivo porcine pancreas," Biomed. Opt. Express **12**(7), 4423–4437 (2021).
56. V. G. Truong, Y. W. Lee, and H. W. Kang, "Effect of optical energy modulation on the thermal response of biological tissue: computational and experimental validations," Biomed. Opt. Express **11**(12), 6905–6919 (2020).

Biomedical Optics EXPRESS

57. X. Xu, T. Mills, J. Brookes, *et al.*, "In vitro evaluation of the safety and efficacy of a high-power 450-nm semiconductor blue laser in the treatment of benign prostate hyperplasia," Lasers Med. Sci. **37**(1), 1–7 (2022).
58. P. Ripley, T. Mills, and J. Brookes, "Measurement of the emission profiles of cylindrical light diffusers using a video technique," Lasers Med. Sci. **14**(1), 67–72 (1999).
59. J. Bak and H. W. Kang, "Temperature-monitored optical treatment for radial tissue expansion," Lasers Med. Sci. **32**(5), 993–999 (2017).
60. W. Small IV, W. Buckley, P. R. Wilson, *et al.*, "Fabrication and characterization of cylindrical light diffusers comprised of shape memory polymer," J. Biomed. Opt. **13**(2), 024018 (2008).
61. A. Franco and I. Velotti, *Development of a laser beam modeling tool for high power applications*, 2020, Politecnico di Torino.
62. H. Vu and J. Lee, "Implementation and Verification of Fresnel Zone Plate Patterns Designed by Optimization of Surface Phase," Journal of the Korean Society for Precision Engineering **41**(1), 79–84 (2024).
63. Y. Lee, M. J. Low, D. Yang, *et al.*, "Ultra-thin light-weight laser-induced-graphene (LIG) diffractive optics," Light: Sci. Appl. **12**(1), 146 (2023).
64. Y. Wang, X. Luo, and S. Li, "Optimal control method of parabolic partial differential equations and its application to heat transfer model in continuous cast secondary cooling zone," Advances in Mathematical Physics **2015**(1), 1–10 (2015).
65. J.C. Mizeret and H.E. van den Bergh, "Cylindrical fiberoptic light diffuser for medical applications," Lasers Surg. Med. **19**(2), 159–167 (1996).
66. H. Luo, G. Yang, and Q. Zhu, "Fiber endface illumination diffuser for endo-cavity photoacoustic imaging," Opt. Lett. **45**(3), 632–635 (2020).
67. M. D. Ta, V. G. Truong, S. Lim, *et al.*, "Comparative Evaluations on Real-Time Monitoring of Temperature Sensors during Endoscopic Laser Application," Sensors **23**(13), 6069 (2023).
68. P. Franz, X. Wang, H. Zhu, *et al.*, "Detection of blackbody radiation during fiber guided laser-tissue vaporization," Biomed. Opt. Express **11**(2), 791–800 (2020).
69. A. Effat, N. Bernards, A. Gregor, *et al.*, "Laser interstitial thermal therapy of lung lesions near large vessels: a numerical study," Biomed. Phys. Eng. Express **9**(3), 035022 (2023).
70. B. Mets, C. Rose-Innes, Z. Lotz, *et al.*, "Comparison of in vivo and ex vivo porcine liver function using the same liver," J. Hepatol. **17**(1), 3–9 (1993).
71. V. V. Volkov, V B Loshchenov, V. I Konov, *et al.*, "Fibreoptic diffuse-light irradiators of biological tissues," Quantum Electron. **40**(8), 746–750 (2010).
72. W. Ageeli, N. Soha, X. Zhang, *et al.*, "Preoperative imaging accuracy in size determination of prostate cancer in men undergoing radical prostatectomy for clinically localised disease," Insights Imaging **14**(1), 105 (2023).